Fuel 381 (2025) 133645

Contents lists available at ScienceDirect

Fuel

journal homepage: www.elsevier.com/locate/fuel

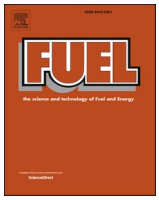

Full Length Article

Comparative effects of plasma and preheating in assisting premixed ammonia/air flames: A DNS study

Mohammad Shahsavari [a], Nilanjan Chakraborty [b], Shenghui Zhong [c], Agustin Valera-Medina [d], Mehdi Jangi [a,*]

[a] Department of Mechanical Engineering, University of Birmingham, United Kingdom
[b] School of Engineering, Newcastle University, United Kingdom
[c] Beihang Hangzhou Innovation Institute Yuhang, China
[d] College of Physical Science and Engineering, Cardiff University, United Kingdom

ARTICLE INFO

Keywords:
Ammonia combustion
Nanosecond-pulsed plasma discharge
Direct numerical simulation

ABSTRACT

In this study, Direct Numerical Simulations are utilized to investigate turbulent premixed NH_3/air flames assisted by two distinct methods: non-equilibrium nanosecond plasma discharges and preheating, while maintaining equal input energy levels for both methods. The results show that plasma is more effective than preheating in increasing the turbulent burning velocity, namely by up to 31% under lean and by 26% in rich conditions. Furthermore, the flame structure is less affected by turbulence when using plasma. A negative correlation between flame displacement speed and local flame curvature is observed for all cases. Furthermore, negatively curved parts of the flame front are dominated by the reaction mode of combustion. In contrast, the positively curved parts are controlled by flame propagation mode in both preheated and plasma-assisted cases. It is shown that, when plasma is utilized, NO emissions are less sensitive to local heat release rate, and the amount of NO emissions is found to be 19% lower in comparison to the preheated case.

1. Introduction

In recent years, increasingly stringent regulations have compelled industries that burn hydrocarbon fuels to reduce their carbon footprint, addressing pressing global warming concerns. One of the most effective strategies for decarbonizing industries involves substituting fossil fuels with carbon-free fuels, such as hydrogen and ammonia. The high cost of hydrogen storage and transportation limits its practical industrial use, especially in countries that rely on hydrogen imports. In contrast, ammonia emerges as a promising near-term alternative due to its well-established mass production processes and cost-effective transportation methods [1,2]. Nevertheless, the relatively lower reactivity of ammonia compared to widely used hydrocarbon fuels has posed challenges in deploying pure ammonia within conventional engines [2].

Several studies have been carried out recently to find methods to enhance ammonia reactivity. Co-burning ammonia with highly reactive fuels, e.g., hydrogen, [3–10] and preheating the reactants [11,12] have proven effective in assisting ammonia combustion. Nevertheless, utilizing such methods comes with drawbacks, such as the high amount of required reactive fuels [13,14] or the need for high preheat temperatures [11,12] to significantly enhance ammonia reactivity. An alternative approach involves using plasma discharges to assist ammonia [15,16] by increasing the concentration of radicals [17], accelerating fuel dissociation [18], and raising the temperature [19]. Recent studies have shown that nanosecond plasma discharge (NSD) can lower the ignition delay time of NH_3/O_2/He and $NH_3/O_2/N_2$ mixtures [20–22]. Besides, in our previous work, we demonstrated that NSDs with pulse energy densities, E_p, exceeding 17 mJ/cm^3, can increase the flame speed of NH_3/air by an order of magnitude [22]. These high-energy discharges affect the flame structure by generating active radicals in the preheat zone [22,23]. Furthermore, discharging NSDs in NH_3/air and NH_3/H_2/air mixtures increases the extinction strain rate of the flames [23]. Plasma can also significantly alter NOx emissions of ammonia flames [22–27]. Previous studies have shown that NSDs increase NOx emissions for low E_p values, while high E_p values can reduce NOx emissions by activating the DeNOx mechanisms in both preheat and post-flame zones [23]. In the aforementioned studies, numerical simulations were conducted using zero and one-dimensional configurations, which did not

* Corresponding author.
E-mail address: m.jangi@bham.ac.uk (M. Jangi).

https://doi.org/10.1016/j.fuel.2024.133645
Received 2 May 2024; Received in revised form 30 October 2024; Accepted 4 November 2024

address the influence of turbulence on the characteristics of plasma-assisted ammonia flames.

While the impact of turbulence on ammonia flames assisted by plasma discharges remains understudied, valuable studies have been carried out to investigate the characteristics of ammonia flames in turbulent flows. Xu *et al.* [28] examined flame-turbulent interactions in high Karlovitz number premixed NH_3/air mixtures using large eddy simulations in the context of the well-stirred reactor modelling. Their findings revealed that changes in the reaction zone thickness are influenced by both flame-turbulence interactions and flow history upstream of the flame front [28]. Through direct numerical simulations, Karimkashi *et al.* [29] analysed the effects of turbulence on NO formation pathways in NH_3/H_2/air mixtures. They demonstrated limited turbulence alterations in NO formation pathways, with curvature playing a role due to the preferential diffusion of H_2 [29]. Netzer *et al.* [30] reported a similar behaviour in laminar NH_3/H_2/air flames, highlighting that the concentration of H radical is high in the positively curved flames (centre of curvature on the fresh mixture side), while it is low in negatively curved flames (centre of curvature on the burned side of the flame). Wiseman *et al.* [13] conducted direct numerical simulations (DNS) on temporally evolving turbulent planar NH_3/H_2/air jet flames, demonstrating that adding hydrogen to NH_3/air flames prevents extinction due to rapid hydrogen diffusion into the preheat layer.

The main objective of this paper is to compare, for the first time, the effects of plasma and preheating on lean and rich NH_3/air flames in a non-decaying turbulent flow using direct numerical simulation. This paper is structured as follows: Section 2 outlines the numerical method and setup, and the obtained results are presented in Section 3, followed by the conclusions in Section 4.

2. Numerical method and setup

2.1. Numerical method

Simulations were performed using an in-house DNS code developed within the OpenFOAM platform [31]. This code solves the conservations of mass, momentum, and energy equations for multispecies and chemically reactive gaseous phases [32–37]. The updated version of the code utilized in this study incorporates the artificial forcing method introduced by Bassenne *et al.* [38] within the momentum equation, Eq. (1), to maintain the turbulent kinetic energy, hence, non-decaying turbulence.

$$\frac{\partial \rho \vec{u}}{\partial t}+\nabla \bullet (\rho \vec{u}\vec{u}) = -\nabla p+\nabla \mu \left(\nabla \vec{u}+(\nabla \vec{u})^T-\frac{2}{3}I\nabla \vec{u} \right)+\rho A\left(\vec{u}-\vec{u}_{Ave} \right) \tag{1}$$

where, ρ is the density, $\vec{u}$ is the velocity vector, p is the pressure, μ is viscosity, A is the forcing coefficient, and $\vec{u}_{Ave}$ is the averaged value of the velocity vector in the computational domain. Here, the forcing coefficient was defined as below,

$$A = \frac{\varepsilon(t) - G[k(t) - k_\infty]/t_{l,\infty}}{2k(t)} \tag{2}$$

where, ε is the turbulent dissipation, k is the averaged value of the kinetic energy in the computational domain, k_∞ is the target value of the kinetic energy, and $t_{l,\infty}/G$ is the time constant, which is on the order of the numerical time step size.

Ludwig-Soret effects were included in the calculation of diffusion velocity. To determine transport properties, including individual diffusion coefficients for each species, we utilized the logarithm polynomial fitting method with the third-order polynomial fits [39]. Using this polynomial consistently yielded fitting errors of less than one percent. Viscosity was computed using the semi-empirical Wilke formula [40], and thermal conductivity was determined by accounting for the differential diffusion effects. In terms of numerical discretization, this study employed a second-order implicit method for time derivatives, while second-order central difference schemes with fourth-order interpolations were used to discretize the convection and diffusion terms.

The plasma modelling in this study was based on the scale separation assumption, where the time scales of non-equilibrium electron-impact reactions are significantly different from thermal reactions by orders of magnitude. This separation allows for the efficient computation of chemical reactions, thus reducing computational cost. Previous studies have shown that discharging plasma upstream of a premixed flame is more effective than placing it within the flame or in post-flame zones [41]. On this basis, the modelling of plasma cases was divided into two phases. First, the fresh mixture, stimulated with NSDs, was modelled in a constant-volume reactor while considering both thermal and plasma kinetics. This was achieved by coupling the open-source Boltzmann equation solver, ZDPlaskin [42], with Cantera codes [43]. ZDPlaskin handled the chemical reactions during plasma discharges, while Cantera dealt with the subsequent thermal phase. During this initial phase, the mutual interactions between turbulence and plasma chemistry were neglected because the time scales of electron impact reactions and turbulence differed by several orders of magnitude. The time scale of the small-scale turbulence structures ranged from 0.1-0.15 ms, whereas electron impact reaction occurred on the nanosecond scale. Here, plasma pulses were represented as square-shaped waves, and each pulse was accurately resolved using adaptive time refinement to account for both electron-impact and chemical reactions. We had extensively validated this methodology in our previous studies on plasma-assisted ammonia and ammonia/hydrogen combustion [22,23]. Following the simulation of the plasma phase for the entire duration of plasma discharges, the resulting mixture was used to uniformly initialize the "fresh reactants" on the sides of the computational domain used for CFD simulations, shown in Fig. 3 (b). Considering the scale separation assumption, the plasma kinetics were not included in the CFD simulations.

The thermal kinetics of ammonia in air were simulated using the mechanisms established by Han *et al.* [44] which comprises 35 species and 177 elementary reactions. Our previous studies showed that this mechanism is an accurate and computationally efficient mechanism for predicting the characteristics of ammonia combustion [22,23]. Additionally, for modelling the plasma kinetics, we utilized a mechanism developed in our previous study [23]. This mechanism combines the one presented by Faingold *et al.* for NH_3/O_2/He [18] with the plasma reactions for N_2 and H_2 derived from the investigations conducted by Zhong *et al.* [45] and Mao *et al.* [46], respectively. Moreover, cross-sections data was obtained from the LXCat database [47] to account for electron-species collisions.

The utilised DNS code has been validated extensively in premixed combustion for different mixtures, namely NH_3/CH_4/air, n-heptane/air, and ethanol/air [34–37,48,49]. However, to further show the accuracy of the code in pure ammonia combustion, a one-dimensional freely propagating laminar flame was simulated, and the results are compared with those obtained with Cantera while keeping the grid size identical in the simulations. Fig. 1 shows the schematic view of the numerical setup. Zirwes *et al.* used a similar configuration to validate EBIdnsFoam code, the other well-validated DNS solver developed for reacting flows within the OpenFOAM platform [50]. Here, the fresh lean NH_3/air mixture at the equivalence ratio of 0.8 enters the domain from the inlet boundary condition. The inlet mixture velocity was fixed at the laminar flame

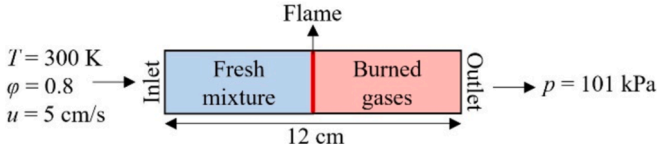

Fig. 1. Computational domain used for one-dimensional freely propagating flame simulations.

speed of the mixture, and the inlet mixture temperature was set at 300 K. Furthermore, the mass fractions of reactants, including NH_3, O_2, and N_2, were fixed at the inlet. Additionally, the zero-gradient boundary condition was used for all other variables. For the outlet, the pressure was fixed at 101325 Pa, and the zero-gradient boundary condition was used for all other variables.

Fig. 2 shows the spatial variations of temperature, heat release rate, and mass fractions of major and some key minor species. Here, the spatial location involves an offset to keep the location at which the maximum heat is released, i.e., $X_{Max\ HRR}$, at the origin. The results show that the code well reproduces the key chemical features of the laminar ammonia flame.

2.2. Numerical setup

The initial conditions for the simulations included a mixture temperature of 298 K and a pressure of 1.0 atm. Equivalence ratios of 0.8 and 1.2 were specifically chosen to assess the influence of equivalence ratio on plasma-assisted and preheated ammonia flames. The mole fraction of oxygen in the oxidizers was set to 0.21. The choice of plasma type and settings was based on the configuration of plasma generators commonly used in the literature [51,52]. Non-equilibrium nanosecond plasma has a well-documented track record for being highly effective in assisting combustion [17,18]. In plasma-assisted flames, we discharged 100 ns plasma pulses with a pulse repetition frequency, *PRF*, of 50 kHz, a reduced electric field, *E/N*, of 350 Td, and $E_p = 5$ mJ/cm^3. The width of each pulse was adapted to achieve the specified E_p. Our previous studies have demonstrated the efficacy of these plasma settings in plasma-assisted NH_3/air combustion [22].

To compare the impact of plasma and preheating on ammonia combustion, we extended our simulations to include preheated NH_3/air mixtures. In this scenario, the initial mixture temperature was set to 678.2 K for the lean mixture and 669.2 K for the rich mixture. These temperatures correspond to a molar thermodynamic preheating energy of 12.2 kJ/mol, matching the total discharged energy utilized in the plasma cases.

The three-dimensional computational domain, as shown in Fig. 3(a), has dimensions of 19.8 × 10 × 10 mm^3 in the x, y, and z directions, respectively. This configuration was selected to make sure that the computational domain in the x-direction is at least an order of magnitude larger than the thickness of the selected flames. The aspect ratios of the computational domain length in the x direction compared to the y and z directions fall within the range commonly used in previous DNS studies [51–55]. The computational domain was initially divided into burned gases at the centre, surrounded by fresh reactants, as shown in Fig. 3(b). Using this configuration, two flame fronts propagate in the fresh reactant. Fig. 3(b) shows these flame fronts by using the *iso*-lines of $c = c^*$, where c is the progress variable defined below,

$$c = \frac{Y_{H_2O}}{Y_{H_2O,eq}} \tag{3}$$

where, Y_{H_2O} and $Y_{H_2O,eq}$ represent the mass fractions of the H_2O molecule and its' corresponding value at the equilibrium condition, and c^* is the progress variable at which heat release reaches its maximum value. Fig. 3(b) also shows the spatial distributions of the temperature and heat release rate at a cross-section of the computational domain.

A similar configuration was used previously by Jangi *et al.* [56] to study auto-ignition and flame propagation in H_2/air mixtures. Here, the composition and thermodynamic state of the "burned" gases at the domain's centre were determined through one-dimensional simulations of freely propagating unassisted laminar NH_3/air flames under the conditions of 298 K and 1.0 atm. As shown in Fig. 3(b), periodic boundary conditions were applied to all boundaries of the computational domain consistent with flame propagation in a constant volume chamber. To introduce turbulence, we employed the Passot-Pouquet method [57] to generate homogenous isotropic turbulence with velocity fluctuations, u', of 5.5 m/s at the initial condition. Here, the Kolmogorov length scale, η, calculated by using [58]

$$\eta = Re_t^{-0.75} l_t \tag{4}$$

where l_t is the integral length scale defined below,

$$Re_t = \frac{u' l_t}{S_L \delta_L} \tag{5}$$

where Re_t is the turbulent Reynolds number, which was set to 118. The laminar flame speed, S_L, and the laminar flame thickness, δ, are obtained through one-dimensional simulations of freely propagating flames. Further details of the computational parameters, including the Kolmogorov length scale as well as the Karlovitz and Damköhler numbers for the investigated cases, are presented in Table 1. Furthermore, the selected cases are shown in the Peters-Borghi diagram in Fig. 4. The selected turbulent level falls within the range typically observed in internal combustion engines [59] and aligns with those used in previous studies on turbulent premixed ammonia/air flames [28]. From the data in Table 1, unassisted ammonia flames exhibit significantly different Karlovitz (*Ka*) and Damköhler (*Da*) numbers compared to pre-heated or plasma-assisted flames. This is typical characteristic of ammonia flames as reported in previous studies, e.g., the reported Ka number in reference [28] ranges from 240 to 3000, and is due to their much lower flame speed and considerably greater flame thickness. Consequently, under a given turbulent condition, they typically display an order of magnitude difference in *Ka* and *Da* numbers relative to their assisted counterparts or typical hydrocarbon fuels. The peak wavenumber was selected to ensure that at least five integral length scales were present within each direction. Fig. 3(a) depicts the spatial distribution of velocity magnitude at a cross-section of the computational domain.

The computational domain was discretized using Cartesian grids,

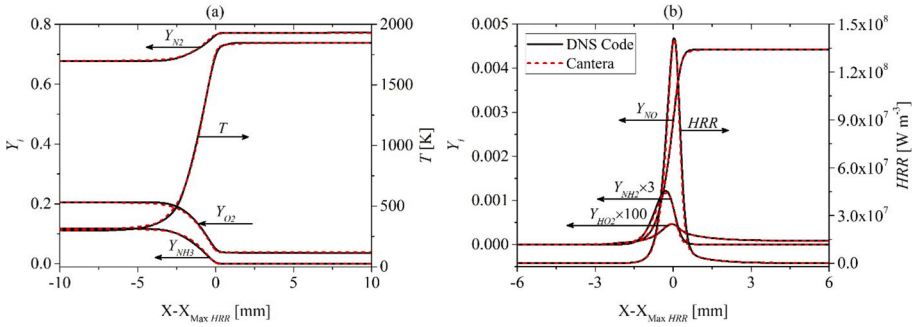

Fig. 2. Spatial profiles of (a) major species and temperature, and (b) minor species and heat release rate predicted by the DNS code (Solid black-line) and Cantera (red dash-line). (For interpretation of the references to colour in this figure legend, the reader is referred to the web version of this article.)

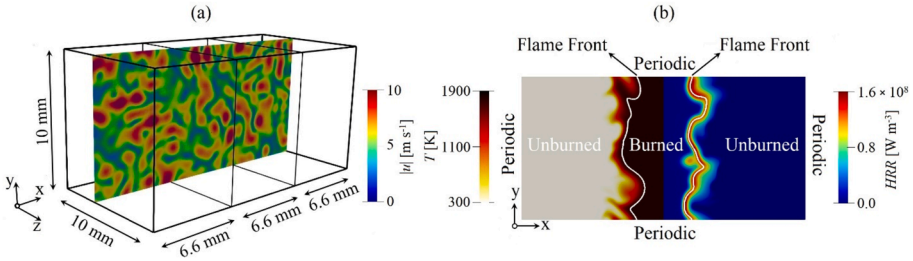

Fig. 3. (a) Computational domain and spatial distribution of the velocity magnitude at a cross-section of the computational domain and (b) spatial distributions of temperature (left) and heat release rate (right) alongside the flame fronts shown by *iso*-lines of $c = c^*$.

Table 1
Key parameters of the unassisted lean (UAL), unassisted rich (UAR), preheated lean (PRL), preheated rich (PRR), plasma-assisted lean (PAL), plasma-assisted rich (PAR) cases; φ is the equivalence ratio, T_{in} is the initial mixture temperature, N is the number of NSD, S_L is the laminar flame speed, δ is the flame thickness, η is the Kolmogorov length scale, Ka is the Karlovitz number, and Da is the Damköhler number.

Properties	UAL	UAR	PRL	PRR	PAL	PAR
φ	0.8	1.2	0.8	1.2	0.8	1.2
T_{in} [K]	300	300	678.2	669.2	300	300
N	0	0	0	0	100	100
S_L [cm/s]	5.0	8.0	38.3	43.4	34.2	43.4
δ [mm]	2.2	1.8	0.9	1.0	1.1	1.1
η[mm]	0.065	0.086	0.203	0.249	0.225	0.286
Ka	1131.9	440.6	19.0	14.8	23.8	14.8
Da	0.0096	0.0247	0.571	0.733	0.456	0.733

employing a uniform grid spacing of 50 μm. With this grid resolution, the thermal flame thickness was resolved with at least 17 grids, while the Kolmogorov length scale was resolved precisely. The utilized grid resolution aligns with the typical ranges used in the literature for DNS of premixed flames [13,60–63].

3. Results and discussions

3.1. Bulk flame features

Fig. 5(a) and (b) show the time history of the turbulent burning velocity, S_T, and the flame surface area, A_T, for the investigated cases. In these figures, S_T and A_T are non-dimensionalised by the S_L, the laminar flame speed, and A^0, the computational domain cross-section area:$4.5\delta_0 \times 4.5\delta_0$, respectively. Here, S_T and A_T were calculated as follows,

$$S_T = \frac{1}{\rho_u A^0} \int \dot{\omega}_c dV \tag{6}$$

$$A_T = \int |\nabla c| dV \tag{7}$$

where, ρ_u is the density of the unburned gases, $\dot{\omega}_c$ is the reaction rate of progress variable, and V is the volume of the computational domain.

Fig. 5(a) shows that S_T of plasma cases (PAL and PAR) assumes greater values than that of the preheated cases (PRL and PRR) consistently throughout the simulation. In contrast, those of the unassisted flames (UAL and UAR) decrease after approximately 1 ms from the start of the simulation, indicating a global flame extinction of the unassisted flames. The results reveal that plasma increases the turbulent flame speed of the selected mixtures, achieving at least 31 % higher S_T/S_L in the lean mixture and 26 % higher S_T/S_L in the rich mixture when compared to the preheated cases. Meanwhile, Fig. 5(b) shows that the flame surface areas of the unassisted cases are initially quite substantial but monotonically decrease until they eventually extinguish, which can be due to the significant temperature difference between the burned and unburned gases in unassisted flames established at the initial conditions. Comparing the preheated and plasma cases shows that A_T of the preheated cases consistently remains higher than that of the plasma cases.

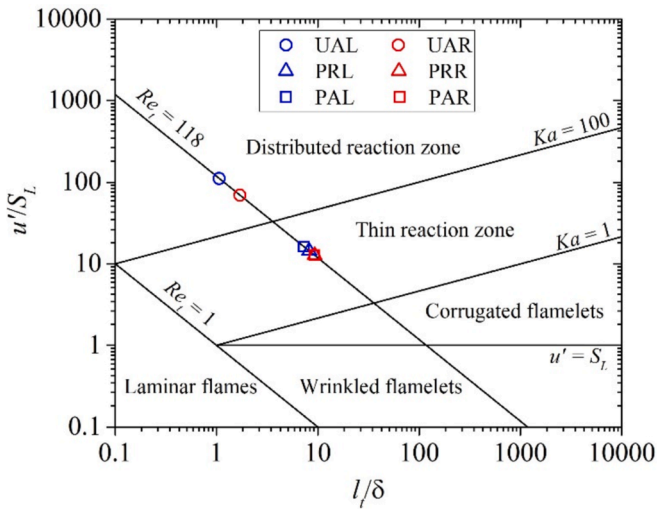

Fig. 4. Simulated cases in the turbulent premixed regime diagram.

3.2. Microscopic flame features

In this section, we compare the behaviour of plasma and preheated flames at the microscopic level. Comparing the characteristics of the preheated and plasma-assisted flames presented in Fig. 5, it can be found that the relative differences in flame characteristics between preheated and plasma-assisted flames are nearly constant for time > 1 ms. For instance, the ratio of the non-dimensionalised turbulent burning velocity in plasma-assisted lean flame to that of the preheated lean flame, i.e., $(S_T/S_L)_{PAL}/(S_T/S_L)_{PRL}$, is in the range of 1.303–1.31 at 1 < time < 2 ms. Therefore, the results presented in this section are obtained at a single time instant, i.e., time = 1.8 ms, after which unassisted flames are extinguished.

Fig. 6(a) and (b) show distributions of the conditional mean values of heat release rate as a function of the progress variable for lean and rich mixtures, respectively. Additionally, profiles of heat release rate for laminar cases are provided in Fig. 6(a) and (b) for the reference, which were obtained through one-dimensional simulations of freely propagating flames using Cantera. It can be seen that in laminar flames, both preheating and NSDs significantly increase the heat release rate, especially in the case of preheating, with factors of 5.2 and 4 for lean and rich mixtures, respectively. In comparison, the utilization of plasma raises the heat release rate by factors of 3.2 and 2.4 for lean and rich mixtures, respectively. These enhancements coincide with a shift of the maximum heat release rate toward the lower progress values compared to the unassisted flames. Fig. 6(a) and (b) show that the introduction of

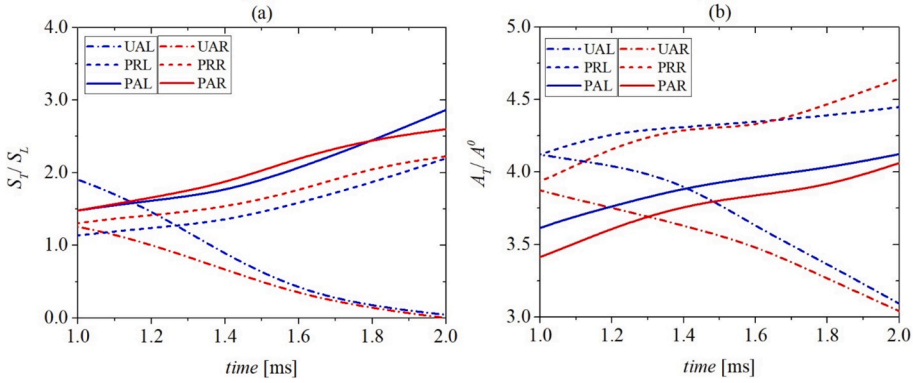

Fig. 5. Time history of non-dimensionalised (a) turbulent burning velocity and (b) flame surface area for unassisted, preheated, and plasma-assisted flames.

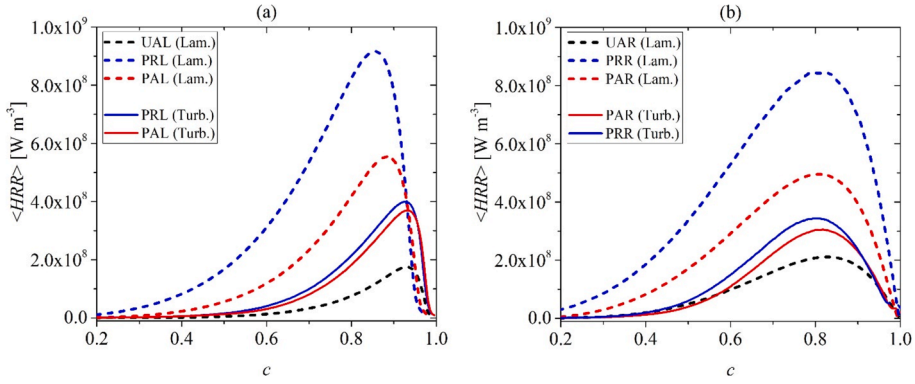

Fig. 6. Dependency of the conditional mean of heat release rate on progress variable for (a) lean and (b) rich mixtures.

turbulence leads to a deterioration in the heat release rate in both lean and rich cases, aligning with findings previously reported by Ichimura *et al.* [64] concerning strained NH_3/air flames. The results show that such deteriorations are dramatically higher in the preheated flames compared to the plasma-assisted ones, which indicates that using plasma recoups part of the heat release reduced by turbulence. This observation underscores the role of radical pools generated by NSDs in enhancing thermal reactions, as demonstrated in our previous work [23]. These radicals appear to compensate for the disruptive effects of turbulence in transporting heat away from the reaction zone. To further investigate the effects of plasma and preheating on the ammonia flame front, analyses were conducted at $c = c^*$.

Fig. 7 displays the *iso*-surface of c^* for PRL (Fig. 7(a)), PRR (Fig. 7(b)), PAL (Fig. 7(c)), and PAR (Fig. 7(d)) cases, coloured by the flame displacement speed, S_d (Fig. 7(I)), the curvature, κ, (Fig. 7(II)), Y_H, (Fig. 7(III)), and combustion index, *IND*, (Fig. 7(IV)), with S_d, κ, and *IND* defined as follows:

$$\kappa = \nabla \bullet \vec{n} \tag{8}$$

$$S_d = S_r + S_n + S_t \tag{9}$$

$$IND = \frac{|D_c|}{R_c} - \frac{|A_c|}{R_c} \tag{10}$$

In these equations, $\vec{n}$ is the flame normal vector, pointing toward the unburned gases, and D_c, A_c, and R_c denote the diffusion, advection, and reaction source terms of the reaction progress variable transport equation. Moreover, S_r, S_n, and S_t are the contributions of the reaction, normal diffusion, and tangential diffusion in S_d, respectively, calculated as follows [60,65,66].

$$n = -\frac{\nabla c}{|\nabla c|} \tag{11}$$

$$S_r = \frac{\dot{\omega}_c}{\rho|\nabla c|} \tag{12}$$

$$S_n = -\frac{1}{\rho|\nabla c|} n \bullet \nabla(\rho D|\nabla c|) \tag{13}$$

$$S_t = -D\kappa \tag{14}$$

Although only the flame propagation modes are predominantly obtained in conventional premixed flames, the presence of radicals in the plasma-assisted flames or mixture activation due to temperature augmentations by preheating can give rise to the possibility of reaction-dominant events. Here, the combustion index is utilised to distinguish the flame propagation mode from the reaction dominant mode. In this context, the latter is deemed to occur when the advection of the progress variable significantly exceeds its diffusion, i.e., $IND \approx -1$. To enhance the readability of Fig. 7(IV), the *IND* contour is plotted with a range between -1 and 1 by setting the contour's minimum and maximum values to -1 and 1, respectively. The results demonstrate that when compared to plasma cases, the preheated flame experiences severe local extinctions. Additionally, S_d assumes relatively high values for $\kappa < 0$. We calculated the cross-correlation coefficient between S_d and κ on $c = c^*$ for the selected cases. The results show that the correlation coefficient, i.e., $cc(S_d, \kappa)$, is smaller than -0.4 for all cases, indicating that S_d negatively correlates with κ in all cases. Analyses not presented here show that increases in S_d for $\kappa < 0$ are accompanied by a noticeable drop in the reaction rate of the fuel in the negatively curved parts of the flame, matching Zirwes *et al.*'s numerical results on H_2/air flames [67].

Importantly, Fig. 7(II) and (III) show that Y_H is approximately

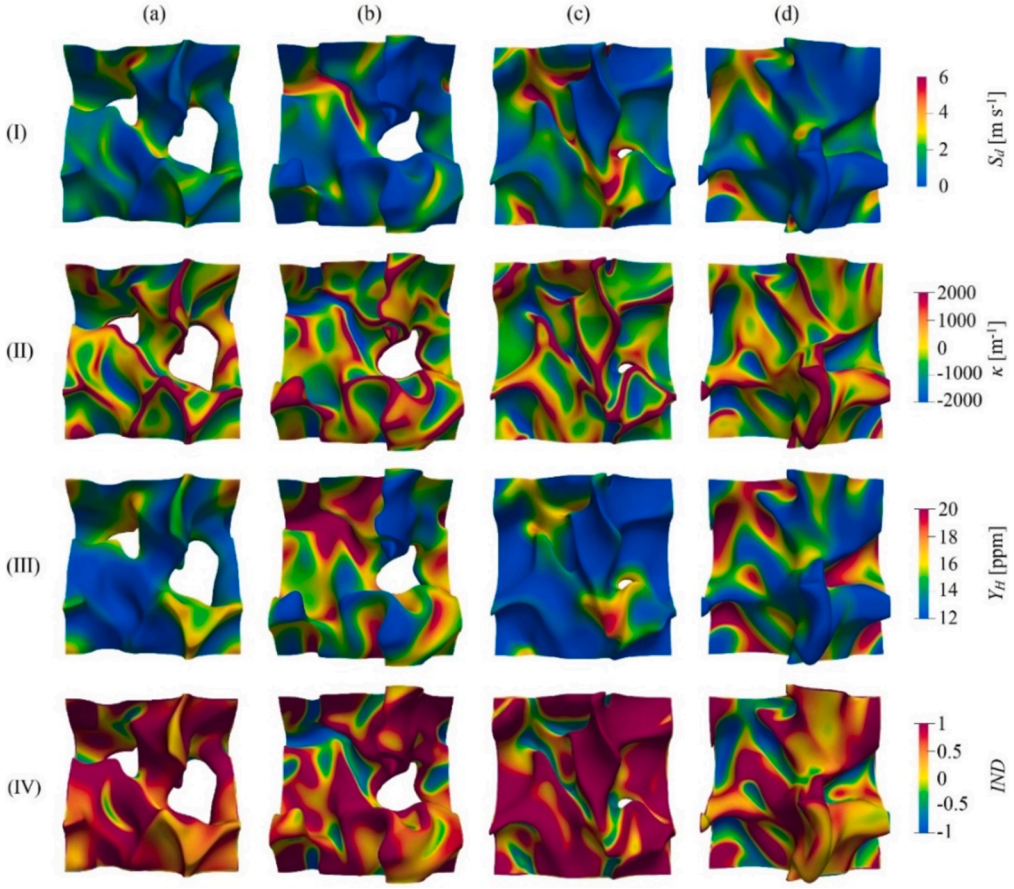

Fig. 7. Premixed flame fronts in (a) PRL, (b) PRR, (c) PAL, and (d) PAR cases coloured with (I) S_d, (II) κ, (III) Y_H, and (IV) *IND*.

negatively correlated with κ. This observation is not in line with the findings of Netzer *et al.* [30] for laminar flames, where they reported that high Y_H was consistently associated with the positively curved part of the flame, and low Y_H was found in the negatively curved part of the flame. Fig. 7(IV) reveals the underlying mechanism behind the discrepancies between the present results and those reported by Netzer *et al.* [30]. It shows that there are several reaction-dominant events in the negatively curved parts of the flame, i.e., when $\kappa < 0$. These events locally increase Y_H and S_d. This phenomenon is further supported by considering Fig. 8, which provides a closer view of a typical section of the highly negatively curved region of the reaction front, marked a "CN". This region displays a notably large concentration of HO_2 radical, confirming the occurrence of substantial reaction dominant events in the negatively curved parts of the flame front.

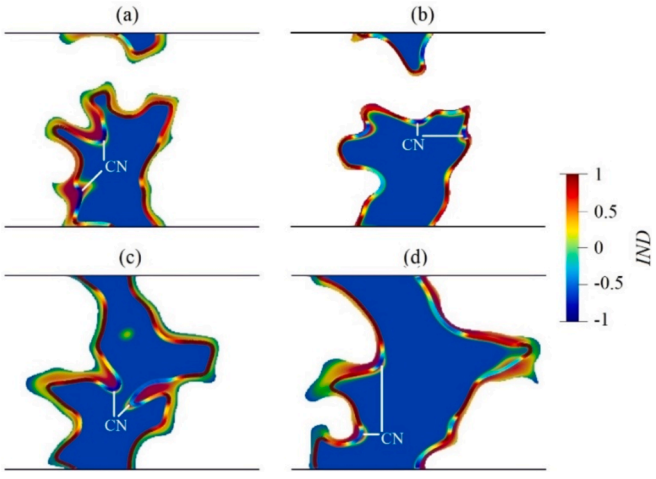

Fig. 8. Spatial distribution of Y_{HO2} (blue to red colours represent minimum to maximum values of Y_{HO2}) and flame front coloured by *IND* for (a) PRL, (b) PRR, (c) PAL, and (d) PAR cases. (For interpretation of the references to colour in this figure legend, the reader is referred to the web version of this article.)

Fig. 9 illustrates the displacement speed and its components, conditioned on $c = c^*$ and non-dimensionalised by S_L, as functions of the curvature for the investigated cases. Results show a consistent pattern across all cases: the reaction and normal diffusion terms nonlinearly depend on the curvature, and the tangential diffusion term negatively correlates with the flame curvature. Considering the noticeable contribution of S_t^* in S_d^*, the dependency on the flame curvature is conveyed to the S_d^*. This is in line with the calculated $cc(S_d, \kappa)$ and the results presented in Fig. 7. These trends are also similar to the previously reported results for hydrocarbon/air flames [68–72]. Echekki and Chen suggested that the effects of curvature on the displacement speed at negative curvature would be due to differential diffusion [68]. By contrast, Chakraborty and co-workers reported a similar trend even in the absence of detailed chemistry, highlighting its significant reliance on fluid dynamic effects [73,74]. Here, we further investigate the effects of detailed chemistry and reaction dominant mode on the correlation between the flame displacement speed and curvature. To such an aim, the scattered data points in Fig. 9 are colour-coded based on the *IND* value using binary red colour for $IND > 0$ and blue for $IND < 0$. In Fig. 9, the black lines show the conditional mean data. In all cases, it is consistently observed that reaction-dominant events predominantly occur in the negatively curved parts of the flame front. Therefore, negatively curved parts of the flame are controlled by the reaction mode of the combustion, which raises the flame displacement speed. On the other hand, the positively curved parts of the flames are dominated by the flame

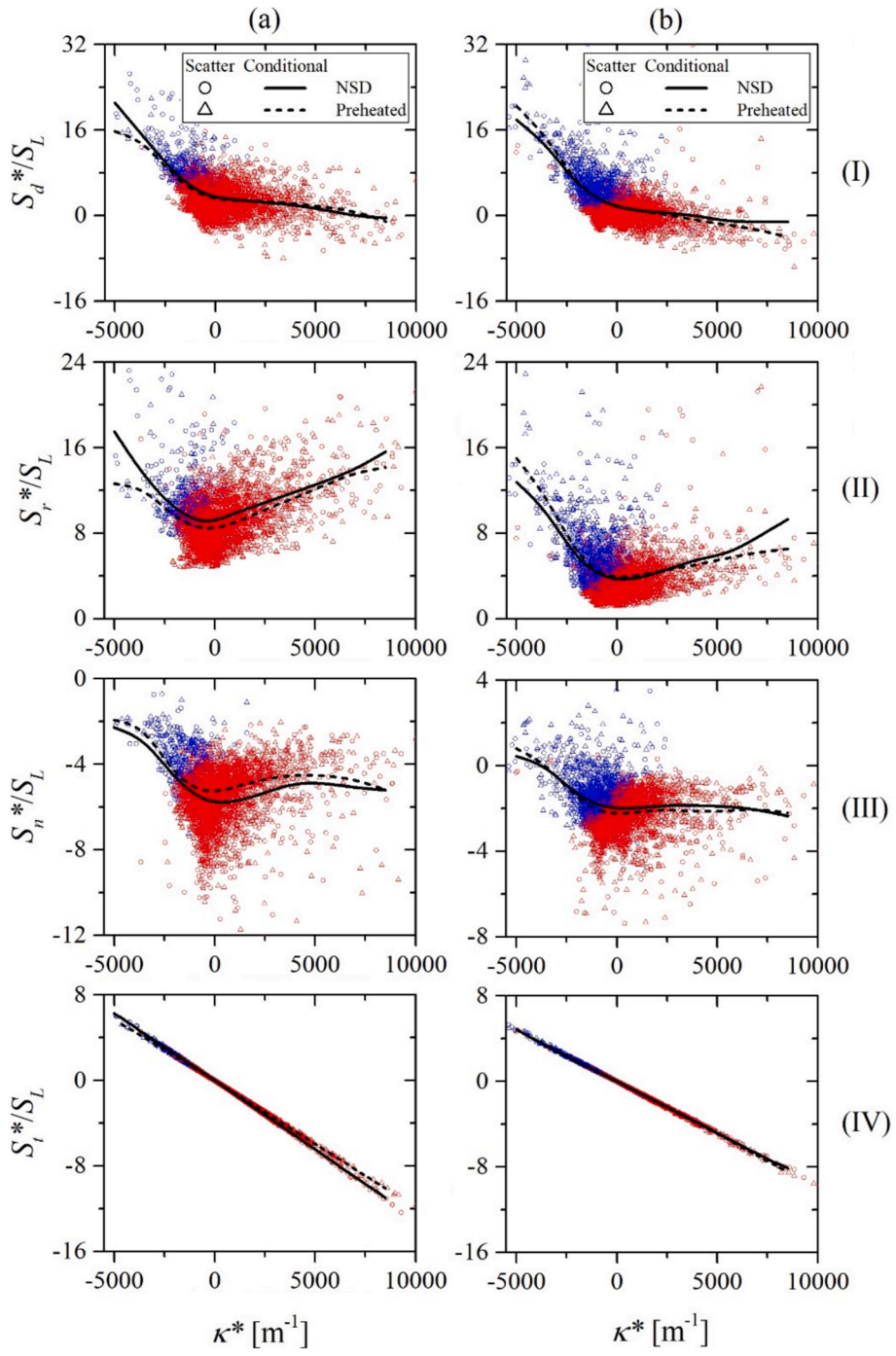

Fig. 9. (I) Conditional displacement speed and its components, including (II) reaction, (III) normal diffusion, and (IV) tangential diffusion, non-dimensionalised by the laminar flame speed as a function of curvature at $c = c^*$ for (a) $\varphi = 0.8$ and (b) $\varphi = 1.2$.

propagation mode. The results reveal that the flame displacement speed is almost identical in preheated and plasma-assisted flames. Nevertheless, the turbulent burning velocity plotted in Fig. 5 is considerably higher in plasma-assisted flame compared to the preheated case.

Using Fig. 9(I), the Markstein number [75] is calculated for the selected cases considering the conditional flame displacement speed. Here, only flame location at which $IND > 0$ is considered in the calculations, corresponding to flame propagation mode. The results show that the Markstein number is 0.14 and 0.17 in lean and rich cases, respectively.

To further evaluate the effects of plasma and preheating on the flame structure, $1/<|\nabla c|^*>$ is plotted as a function of the progress variable in Fig. 10. This quantity can be taken to signify the local flame thickness [72]. The results show that $1/<|\nabla c|^*>$ is higher in plasma-assisted flames than in preheated cases for all curvature values, independent of the equivalence ratio. This is in line with the trend observed for laminar flames, as can be found in Table 1.

Examining the influence of plasma and preheating on NOx emissions in a lean ammonia flame holds significance in both practical applications and fundamental research. This is primarily due to the prevalent formation of NOx in ammonia flames when operating under lean conditions. Fig. 11 shows spatial distributions of the mass fraction of NO and heat release rate in PRL and PAL cases. The results show that the mass fraction of NO is comparatively higher in the preheated case when

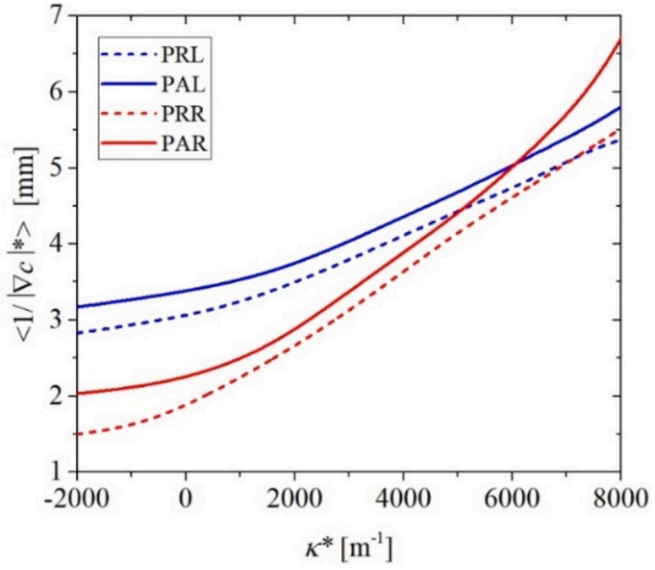

Fig. 10. Conditional mean of $1/<|\nabla c|^*>$ as a function of curvature at $c = c^*$ for PRL, PAL, PRR, and PAR cases using data sets with $IND > 0$.

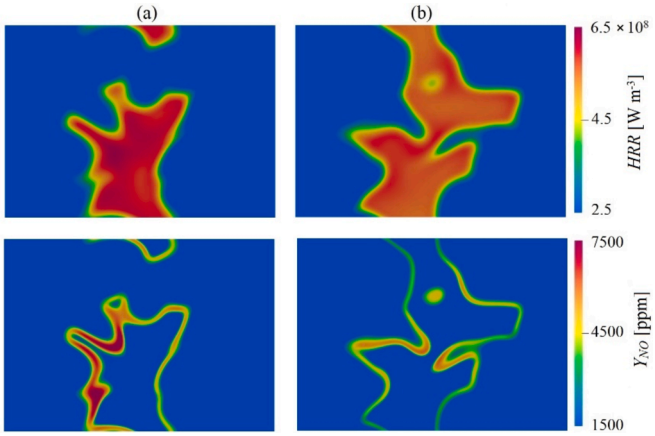

Fig. 11. Spatial distributions of the mass fraction of NO and heat release rate in (a) preheated and (b) plasma-assisted cases.

compared to the plasma case. To quantify this difference, we have computed the volume-integrated NO net production rate per unit heat release, p_{NO}, across the entire computational domain using the following equation.

$$p_{NO} = \frac{\int \dot{\omega}_{NO} dV}{\int HRR dV} \tag{15}$$

where $\dot{\omega}_{NO}$ is the net production rate of NO. Then, the averaged value of p_{NO} was calculated over 1 ms of the simulations. The results show that NO production rates in PRL and PAL flames are 2213 and 1856 mg/MJ, respectively. This highlights the superior performance of discharging plasma over preheating when it comes to NOx emissions. It is known that fuel NOx is the dominant pathway of NO formation in ammonia flames [30]. However, to the best of the authors' knowledge, there is no data available in the literature depicting the effects of plasma discharges on NOx pathways in turbulent ammonia flames. The results presented in Fig. 11 fill this gap by showing that the spatial distribution of the mass fraction of NO weakly correlates with regions accompanied by high heat release rates in both cases. To quantitatively assess the dependency of NO emissions on the heat release rate, the cross-correlation coefficient between the mass fraction of NO and the heat release rate is calculated in these cases. It is found that the cross-correlation coefficient is 0.3216 and 0.0592 for the PRL and PAL cases, respectively. These values suggest that preheating the mixture instead of discharging plasma amplifies the formation of thermal NOx.

Fig. 12 shows the pathways of NO production and consumption in PRL and PAL flames. It is known that NO formation is a post-flame phenomenon with relatively larger time scales compared to turbulence and flame time scales. Considering these properties, the results presented in Fig. 12 were obtained where the mass fraction of NO reaches its maximum value in each case. It can be found that the pathways are remarkably similar between these two cases. However, there are significant differences in the production and consumption rates, with the PAL case exhibiting lower rates compared to the PRL flame. Importantly, it is worth noting that the average temperature at the location where the NO mass fraction peaks is only 3 % higher in the PRL case, while the mass fraction of NO in this case is 19 % higher than that in the PAL flame.

Analysing the mixture properties during the plasma discharges reveals that NSDs dissociate 15 % of NH_3 by volume. During this process, only 506 ppm NO is produced, accounting for 4.5 % of the total NO in the PAL case. This implies that a portion of the fuel that would result in high levels of NO emissions around the flame is instead dissociated by plasma, leading to relatively low NO emissions. Fig. 13 displays the pathways of NO during 100 NSDs. A comparison between Figs. 12 and 13 reveals that NO is primarily produced by $NO_2 + H \rightarrow OH + NO$ near the flame, while $HNO + H \rightarrow NO + H_2$ is the main reaction producing NO during the plasma discharges. In both cases, H plays a pivotal role in NO formation pathways. This radical is produced by two orders of magnitude more near the flame front, resulting in more NO compared to those generated during the plasma discharges.

4. Conclusions

In this paper, three-dimensional direct numerical simulations were carried out to assess the impact of nanosecond plasma and preheating on lean and rich premixed NH_3/air flames in the thin-reaction-zone regime. This is a crucial investigation to quantitatively determine the mechanism of plasma in enhancing flame characteristics of premixed ammonia/air mixtures in applications such as gas turbines or internal combustion engines for the decarbonisation of power production, compared to the more conventional approach, such as preheating. The main findings are listed as follows:

- The displacement speed negatively correlates with the flame curvature in both preheated and plasma-assisted flames.
- The reaction dominant events play a role in raising the H radical and local flame displacement speed in the negatively curved parts of the flame.

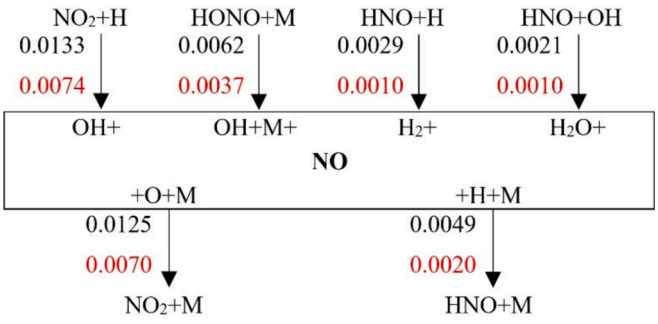

Fig. 12. Rates of production and consumption of NO in [kmol m^{-3} s^{-1}] when the mole fraction of NO is at the maximum value in preheated (black) and plasma-assisted (red) cases. (For interpretation of the references to colour in this figure legend, the reader is referred to the web version of this article.)

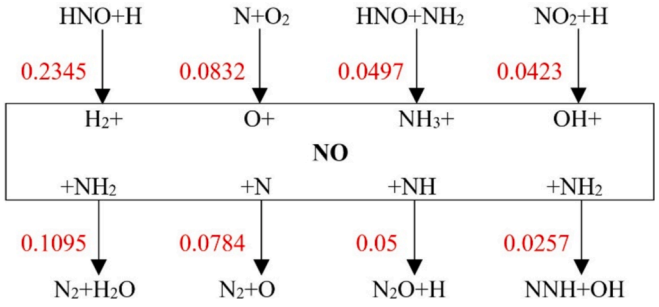

Fig. 13. Rates of production and consumption of NO in [kmol m^{-3} s^{-1}] during 100 NSDs.

- Positively curved parts of the flames are dominated by the flame propagation mode.
- Discharging plasma is more effective than preheating in increasing the turbulent burning velocity of ammonia/air for a given input energy.
- The plasma-assisted flame yields 19 % lower NO compared to the preheated flame. This is attributed to the dissociation of a portion of the fuel via plasma discharges that would otherwise lead to high levels of NO emissions near the flame.

CRediT authorship contribution statement

Mohammad Shahsavari: Writing – review & editing, Writing – original draft, Visualization, Validation, Methodology, Investigation, Formal analysis, Conceptualization. **Nilanjan Chakraborty:** Writing – review & editing, Writing – original draft, Methodology, Investigation. **Shenghui Zhong:** Writing – original draft, Software, Methodology. **Agustin Valera-Medina:** Writing – review & editing, Writing – original draft, Investigation, Conceptualization. **Mehdi Jangi:** Writing – review & editing, Writing – original draft, Supervision, Project administration, Methodology, Investigation, Funding acquisition, Formal analysis, Conceptualization.

Declaration of competing interest

The authors declare that they have no known competing financial interests or personal relationships that could have appeared to influence the work reported in this paper.

Acknowledgements

This study, as a part of the PlasNH3 project, was supported by the Marie Sklodowska-Curie Foundation through MSCA-IF-EF-ST action, H2020-MSCA-IF-2020 call. The computations described in this paper were performed using the University of Birmingham's BlueBEAR HPC service, which provides a High-Performance Computing service to the University's research community. See http://www.birmingham.ac.uk/bear for more details.

Data availability

Data will be made available on request.

References

[1] Kobayashi H, Hayakawa A, Somarathne KDKA, Okafor EC. Science and technology of ammonia combustion. Proc Combust Inst 2019;37:109–33.
[2] Valera-Medina A, Amer-Hatem F, Azad AK, Dedoussi IC, de Joannon M, Fernandes RX, et al. Review on Ammonia as a Potential Fuel: From Synthesis to Economics. Energy Fuels 2021;35:6964–7029.
[3] Okafor EC, Somarathne KDKA, Ratthanan R, Hayakawa A, Kudo T, Kurata O, et al. Control of NOx and other emissions in micro gas turbine combustors fuelled with mixtures of methane and ammonia. Combust Flame 2020;211:406–16.
[4] Colson S, Kuhni M, Hayakawa A, Kobayashi H, Galizzi C, Escudié D. Stabilization mechanisms of an ammonia/methane non-premixed jet flame up to liftoff. Combust Flame 2021;234. https://doi.org/10.1016/j.combustflame.2021.111657.
[5] Zhang X, Moosakutty SP, Rajan RP, Younes M, Sarathy SM. Combustion chemistry of ammonia/hydrogen mixtures: Jet-stirred reactor measurements and comprehensive kinetic modeling. Combust Flame 2021;234. https://doi.org/10.1016/j.combustflame.2021.111653.
[6] Gotama GJ, Hayakawa A, Okafor EC, Kanoshima R, Hayashi M, Kudo T, et al. Measurement of the laminar burning velocity and kinetics study of the importance of the hydrogen recovery mechanism of ammonia/hydrogen/air premixed flames. Combust Flame 2022;236. https://doi.org/10.1016/j.combustflame.2021.111753.
[7] Cai T, Zhao D, Chan SH, Shahsavari M. Tailoring reduced mechanisms for predicting flame propagation and ignition characteristics in ammonia and ammonia/hydrogen mixtures. Energy 2022;260. https://doi.org/10.1016/j.energy.2022.125090.
[8] Zhao H, Zhao D, Becker S, Zhang Y. NO emission and enhanced thermal performances studies on counter-flow double-channel hydrogen/ammonia-fuelled mixrocombustors with oval-shaped internal threads. Fuel 2023;341. https://doi.org/10.1016/j.fuel.2023.127665.
[9] Sun Y, Cai T, Shahsavari M, Sun D, Sun X, Zhao D, et al. RANS simulations of combustion and emission characteristics of a premixed NH3/H2 swirling flame with reduced chemical kinetic model. Chin J Aeronaut 2021;34:17–27.
[10] Chi C, Thevenin D. DNS Study on reactivity stratification with prechamber H2/air turbulent jet flame to enhance NH3/air combustion in gas engines. Fuel 2023;347. https://doi.org/10.1016/j.fuel.2023.128387.
[11] Kurata O, Iki N, Matsunuma T, Inoue T, Tsujimura T, Furutani H, et al. Performances and emission characteristics of NH3–air and NH3CH4–air combustion gas-turbine power generations. Proc Combust Inst 2017;36:3351–9.
[12] Okafor EC, Yamashita H, Hayakawa A, Somarathne KDKA, Kudo T, Tsujimura T, et al. Flame stability and emissions characteristics of liquid ammonia spray co-fired with methane in a single stage swirl combustor. Fuel 2021;287. https://doi.org/10.1016/j.fuel.2020.119433.
[13] Wiseman S, Rieth M, Gruber A, Dawson JR, Chen JH. A comparison of the blow-out behavior of turbulent premixed ammonia/hydrogen/nitrogen-air and methane–air flames. Proc Combust Inst 2021;38:2869–76.
[14] Franco MC, Rocha RC, Costa M, Yehia M. Characteristics of NH3/H2/air flames in a combustor fired by a swirl and bluff-body stabilized burner. Proc Combust Inst 2021;38:5129–38.
[15] Starikovskiy A, Aleksandrov N. Plasma-assisted ignition and combustion. Prog Energy Combust Sci 2013;39:61–110.
[16] Ju Y, Sun W. Plasma assisted combustion: Progress, challenges, and opportunities. Combust Flame 2015;162:529–32.
[17] Wang Y, Guo P, Chen H, Chen Z. Numerical modeling of ignition enhancement using repetitive nanosecond discharge in a hydrogen/air mixture I: calculations assuming homogeneous ignition. J Phys D Appl Phys 2020;54:1–11.
[18] Casey TA, Han J, Belhi M, Arias PG, Bisetti F, Im HG, et al. Simulations of planar non-thermal plasma assisted ignition at atmospheric pressure. Proc Combust Inst 2017;36:4155–63.
[19] Nagaraja S, Li T, Sutton JA, Adamovich IV, Yang V. Nanosecond plasma enhanced H2/O2/N2 premixed flat flames. Proc Combust Inst 2015;35:3471–8.
[20] Faingold G, Lefkowitz JK. A numerical investigation of NH3/O2/He ignition limits in a non-thermal plasma. Proc Combust Inst 2021;38:6661–9.
[21] Taneja TS, Johnson PN, Yang S. Nanosecond pulsed plasma assisted combustion of ammonia-air mixtures: Effects on ignition delays and NOx emissions. Combust Flame 2022;245. https://doi.org/10.1016/j.combustflame.2022.112327.
[22] Shahsavari M, Konnov AA, Valera-Medina A, Jangi M. On nanosecond plasma-assisted ammonia combustion: effects of pulse and mixture properties. Combust Flame 2022;245. https://doi.org/10.1016/j.combustflame.2022.112368.
[23] Shahsavari M, Konnov AA, Bai XS, Valera-Medina A, Li T, Jangi M. Synergistic effects of nanosecond plasma discharge and hydrogen on ammonia combustion. Fuel 2023;348. https://doi.org/10.1016/j.fuel.2023.128475.
[24] Choe J, Sun W, Ombrello T, Carter C. Plasma assisted ammonia combustion: Simultaneous NOx reduction and flame enhancement. Combust Flame 2021;228:430–2.
[25] Lin Q, Jiang Y, Liu C, Chen L, Zhang W, Ding J, et al. Controllable NO emission and high flame performance of ammonia combustion assisted by non-equilibrium plasma. Fuel 2022;319. https://doi.org/10.1016/j.fuel.2022.123818.
[26] Kim GT, Park J, Chung SH, Yoo CS. Effects of non-thermal plasma on turbulent premixed flames of ammonia/air in a swirl combustor. Fuel 2022;323. https://doi.org/10.1016/j.fuel.2022.124227.
[27] Tang Y, Xie D, Shi B, Wang N, Li S. Flammability enhancement of swirling ammonia/air combustion using AC powered gliding arc discharges. Fuel 2022;313. https://doi.org/10.1016/j.fuel.2021.122674.
[28] Xu L, Fan Q, Liu X, Cai X, Subash AA, Brackmann C, et al. Flame/turbulence interaction in ammonia/air premixed flames at high karlovitz numbers. Proc Combust Inst 2023;39:2289–98.
[29] Karimkashi S, Tamadonfar P, Kaario O, Vuorinen V. A Numerical Investigation on Effects of Hydrogen Enrichment and Turbulence on NO Formation Pathways in Premixed Ammonia/Air Flames. Combust Sci Technol 2023;30. https://doi.org/10.1080/00102202.2023.2180634.
[30] Netzer C, Ahmed A, Gruber A, Løvås T. Curvature effects on NO formation in wrinkled laminar ammonia/hydrogen/nitrogen-air premixed flames. Combust Flame 2021;232. https://doi.org/10.1016/j.combustflame.2021.111520.
[31] " The OpenFOAM Foundation," 2020. [Online]. Available: www.openfoam.org.
[32] Poinsot T, Veynante D. Theoritical and Numerical Combustion. Philadelphia: Edwards; 2005.

[33] S. Zhong, "reactingDNS_OpenFOAM," 2023. [Online]. Available: https://github.com/ZSHtju/reactingDNS_OpenFOAM/blob/OpenFOAM8/reactingDNS_equation.pdf.
[34] Zhong S, Zhang F, Jangi M, Bai XS, Yao M, Peng Z. Structure and propagation of n-heptane/air premixed flame in low temperature ignition regime. Appl Energy 2020;275. https://doi.org/10.1016/j.apenergy.2020.115320.
[35] Zhang N, Zhang F, Zhong S, Peng Z, Yu J, Liu H, et al. Numerical and theoretical investigation of ethanol/air flame instability. Combust Theor Model 2020;24:1108–29.
[36] Zhong S, Zhang F, Peng Z, Bai F, Du Q. Roles of CO2 and H2O in premixed turbulent oxy-fuel combustion. Fuel 2018;2018:1044–54.
[37] Zhong S, Zhang F, Du Q, Peng Z. Characteristics of reactivity controlled combustion with n-heptane low temperature reforming products. Fuel 2020;275. https://doi.org/10.1016/j.fuel.2020.117980.
[38] Bassenne M, Urzay J, Park GI, Moin P. Constant-energetics physical-space forcing methods for improved convergence to homogeneous-isotropic turbulence with application to particle-laden flows. Phys Fluids 2016;28. https://doi.org/10.1063/1.4944629.
[39] Kee RJ, Dixon-lewis G, Warnatz J, Coltrin ME, Miller JA, Moffat HK. A Fortran computer code package for the evaluation of gas-phase, multicomponent transport properties. Lewis 1986.
[40] Wilke CR. A viscosity equation for gas mixtures. J Chem Phys 2004;18:517–9.
[41] Yang S, Nagaraja S, Sun W, Yang V. Multiscale modeling and general theory of non-equilibrium plasma-assisted ignition and combustion. J Phys D Appl Phys 2017;50. https://doi.org/10.1088/1361-6463/aa87ee.
[42] Pancheshnyi S, Eismann B, Hagelaar G, Pitchford L. Computer code zdplaskin. LAPLACE, CNRS-UPS-INP, Toulouse, France: University of Toulouse; 2008.
[43] Goodwin D, Speth R, Moffat H, Weber B. Cantera: An object-oriented software toolkit for chemical kinetics, thermodynamics, and transport processes. Version 2.5.1, 2021.
[44] Han X, Lubrano Lavadera M, Konnov AA. An experimental and kinetic modeling study on the laminar burning velocity of NH3+N2O+air flames. Combust Flame 2021;228:13–28.
[45] Zhong H, Mao X, Rousso A, Patrick C, Yan C, Xu W, et al. Kinetic study of plasma-assisted n-dodecane/O2/N2 pyrolysis and oxidation in a nanosecond-pulsed discharge. Proc Combust Inst 2021;38:6521–31.
[46] Mao X, Chen Q, Rousso AC, Chen TY, Ju Y. Effects of controlled non-equilibrium excitation on H2/O2/He ignition using a hybrid repetitive nanosecond and DC discharge. Combust Flame 2019;206:522–35.
[47] "Dutton database," 13 December 2021. [Online]. Available: www.lxcat.net.
[48] Kee RJ, Dixon-Lewis G, Warnatz J, Coltrin ME, Miller JA. A Fortran computer code package for the evaluation of gas-phase multicomponent transport properties. Sandia National Laboratories Report SAND86-8246 1986;13:80401–1887.
[49] Rodolfo RC, Zhong S, Xu L, Bai XS, Costa M, Cai X, et al. Structure and laminar flame speed of an ammonia/methane/air premixed flame under varying pressure and equivalence ratio. Energy Fuels 2021;35:7179–92.
[50] Zirwes T, Sontheimer M, Zhang F, Abdelsamie A, Pérez FEH, Stein OT, et al. Assessment of numerical accuracy and parallel performance of OpenFOAM and its reacting flow extension EBIdnsFoam. Flow Turbul Combust 2023;111:567–602.
[51] Nagaraja S, Sun W, Yang V. Effect of non-equilibrium plasma on two-stage ignition of n-heptane. Proc Combust Inst 2015;35:3497–504.
[52] Manna MV, Sabia P, Ragucci R, de Joannon M. Oxidation and pyrolysis of ammonia mixtures in model reactors. Fuel 2020;264. https://doi.org/10.1016/j.fuel.2019.116768.
[53] Lee H, Dai P, Wan M, Lipatnikov AN. A DNS study of extreme and leading points in lean hydrogen-air turbulent flames – Part I: Local thermochemical structure and reaction rates. Combust Flame 2022;235. https://doi.org/10.1016/j.combustflame.2021.111716.
[54] Rieth M, Gruber A, Williams FA, Chen JH. Enhanced burning rates in hydrogen-enriched turbulent premixed flames by diffusion of molecular and atomic hydrogen. Combust Flame 2022;239. https://doi.org/10.1016/j.combustflame.2021.111740.
[55] Tian T, Song C, Wang H, Xu C, Luo K, Fan J. The effects of turbulence on the flame structure and NO formation of ammonia turbulent premixed combustion at various equivalence ratios. Fuel 2023;332. https://doi.org/10.1016/j.fuel.2022.126127.
[56] Jangi M, Yu R, Bai XS. A multi-zone chemistry mapping approach for direct numerical simulation of auto-ignition and flame propagation in a constant volume enclosure. Combust Theor Model 2012;16:221–49.
[57] Passot T, Pouquet A. Numerical simulation of compressible homogeneous flows in the turbulent regime. J Fluid Mech 1987;181:441–66.
[58] Fan Q, Liu X, Xu L, Subash AA, Brackmann C, Alden M, et al. Flame structure and burning velocity of ammonia/air turbulent premixed flames at high Karlovitz number conditions. Combust Flame 2022;238. https://doi.org/10.1016/j.combustflame.2021.111943.
[59] Gimenez B, Melgar A, Horrillo A, Tinaut FV. A correlation for turbulent combustion speed accounting for instabilities and expansion speed in a hydrogen-natural gas spark ignition engine. Combust Flame 2021;223:15–27.
[60] Suillaud E, Truffin K, Colin O, Veynante D. Direct Numerical Simulations of high Karlovitz number premixed flames for the analysis and modeling of the displacement speed. Combust Flame 2022;236. https://doi.org/10.1016/j.combustflame.2021.111770.
[61] Wang H, Hawkes ER, Chen JH, Zhou B, Li Z, Aldén M. Direct numerical simulations of a high Karlovitz number laboratory premixed jet flame – an analysis of flame stretch and flame thickening. J Fluid Mech 2017;815:511–36.
[62] Lee HC, Dai P, Wan M, Lipatnikov AN. Influence of molecular transport on burning rate and conditioned species concentrations in highly turbulent premixed flames. J Fluid Mech 2022;928. https://doi.org/10.1017/jfm.2021.794.
[63] Trisjono P, Pitsch H. A direct numerical simulation study on NO formation in lean premixed flames. Proc Combust Inst 2017;36:2033–43.
[64] Ichimura R, Hadi K, Hashimoto N, Hayakawa A, Kobayashi H, Fujita O. Extinction limits of an ammonia/air flame propagating in a turbulent field. Fuel 2019;246:178–86.
[65] Chakraborty N, Cant RS. Influence of Lewis number on strain rate effects in turbulent premixed flame propagation. Int J Heat Mass Transf 2006;49:2158–72.
[66] Chakraborty N. Comparison of displacement speed statistics of turbulent premixed flames in the regimes representing combustion in corrugated flamelets and thin reaction zones, Physics of Fluids, vol. 19, Issue 10, 2007.
[67] Zirwes T, Zhang F, Bockhorn H. Memory effects of local flame dynamics in turbulent premixed flames. Combust Flame 2023;39:2349–58.
[68] Echekki T, Chen JH. Analysis of the contribution of curvature to premixed flame propagation. Combust Flame 1999;118:308–11.
[69] Echekki T, Chen JH. Unsteady strain rate and curvature effects in turbulent premixed methane-air flames. Combust Flame 1996;106:184–202.
[70] Ozel-Erol G, Klein M, Chakraborty N. Lewis number effects on flame speed statistics in spherical turbulent premixed flames. Flow Turbul Combust 2021;106:1043–63.
[71] Klein M, Chakraborty N, Jenkins KW, Cant RS. Effects of initial radius on the propagation of premixed flame kernels in a turbulent environment. Phys Fluids, Vol. 18, Issue 5, 2006.
[72] Aspden AJ, Day MS, Bell JB. Towards the distributed burning regime in turbulent premixed flames. J Fluid Mech 2019;871:1–21.
[73] Chakraborty N, Cant RS. Unsteady effects of strain rate and curvature on turbulent premixed flames in an inflow–outflow configuration. Combust Flame 2004;137:129–47.
[74] Chakraborty N, Klein M, Cant RS. Stretch rate effects on displacement speed in turbulent premixed flame kernels in the thin reaction zones regime. Combust Flame 2007;31:1385–92.
[75] Zhang F, Zirwes T, Habisreuther P, Bockhorn H. Effect of unsteady stretching on the flame local dynamics. Combust Flame 2017;175:170–9.